(p,n) reaction for $89 < A < 130$ and an anomalous optical model potential for sub-Coulomb protons

C. H. Johnson
Oak Ridge National Laboratory, Oak Ridge, Tennessee 37830

A. Galonsky
Michigan State University, East Lansing, Michigan 48824

R. L. Kernell
Old Dominion University, Norfolk, Virginia 23508

(Received 14 May 1979)

The (p,n) cross sections were measured from about 2.5 to 5.8 MeV with about 100-keV target resolution for natural Pd, Ag, Cd, In, and Te and for ^{89}Y, ^{93}Nb, ^{103}Rh, ^{105,106,108,110}Pd, ^{107,109}Ag, ^{111,112,113,114,116}Cd, and ^{125,126,128,130}Te. Systematic uncertainties are about $\pm 2\%$ for ^{89}Y, ^{93}Nb, and the natural targets and about $\pm 4\%$ for the other nuclei. The isotopic $\sigma_{p,n}$ are fitted by adjustment in the depth W_D and diffuseness a_D of the surface imaginary part of a proton optical model potential (OMP) that was chosen previously to describe precision (p,n) data for isotopes of Sn. The diffuseness a_D is found to be nearly constant, about 0.4 fm, but the depth W_D shows a large and systematic A dependence. A study of the parameter space indicates that at least one OMP parameter must have a strong A dependence and that W_D is probably the only such single parameter that will suffice. The explanation of this anomaly is currently unclear.

NUCLEAR REACTIONS: Pd, Ag, Cd, In, Te, natural targets; and ^{89}Y, ^{93}Nb, ^{103}Rh, ^{105,106,108,110}Pd, ^{107,109}Ag, ^{111,112,113,114,116}Cd, ^{125,126,128,130}Te, enriched isotopic targets, $E = 2.5$ to 5.8 MeV, target resolution ~ 100 keV. Measured $\sigma_{p,n}$. Deduced optical model parameters.

INTRODUCTION

This work, which was summarized in a Letter,[1] is a study of medium weight nuclei in search of broad resonances in the proton strength function such as observed so far[2,3] only for the Sn isotopes. For the Sn isotopes Johnson *et al.*[2,3] measured precision (p,n) cross sections at sub-Coulomb energies (3 to 7 MeV), corrected for γ-ray and proton emission to obtain total reaction cross sections, fitted these cross sections with a proton optical model potential (OMP), and divided out the energy dependence of Coulomb penetration from the observed and fitted cross sections to reveal the nuclear effects. The resulting fitted curves for five isotopes from ^{117}Sn to ^{124}Sn are reproduced in Fig. 1(a). The ordinate $\langle S_p \rangle$, which is defined in Sec. IV D, is essentially the total reaction cross section divided by a $(2l+1)$-weighted sum of Coulomb penetration factors. Each curve exhibits a broad resonance; the peak energies shift systematically with increasing size of the nucleus. In the OMP these resonances result from the $3p$ state, which is quasibound by the combined real well and Coulomb potential and broadened by the imaginary potential.

It is reasonable to expect $3p$ resonances to be observed also in neighboring nuclei and to be described by the same OMP as for Sn, with minor adjustments in the parameters. To predict the curves in Fig. 1(a) for the nuclei studied here we have modified this OMP only by including conventional isospin and Coulomb dependences such that the depth of the real well increases 3% from ^{89}Y to ^{130}Te. (Section IV includes the parameters.) The predicted peak moves from 6.3 MeV for ^{89}Y to 5.3 MeV for ^{130}Te. This slow decrease demonstrates the nearly compensating effects of the increasing volume of the real nuclear well and the increasing repulsion of the Coulomb potential. (As a consequence the predicted "size" resonance of $\langle S_p \rangle$ versus A for a fixed energy would be very broad. By comparison, the neutron $3p$ size resonance near $A = 95$, observed, for example, by Camarda,[4] is relatively narrow.)

The mass region was included in a broader survey of (p,n) reactions by Schiffer and Lee[5] and by Elwyn, Marinov, and Schiffer.[6] Using thick targets of natural elements, they measured cross sections with ±10% relative and ±20% absolute uncertainties in 0.5-MeV steps from about 3 to 6 MeV (for our mass region). Their reduced (p,n)

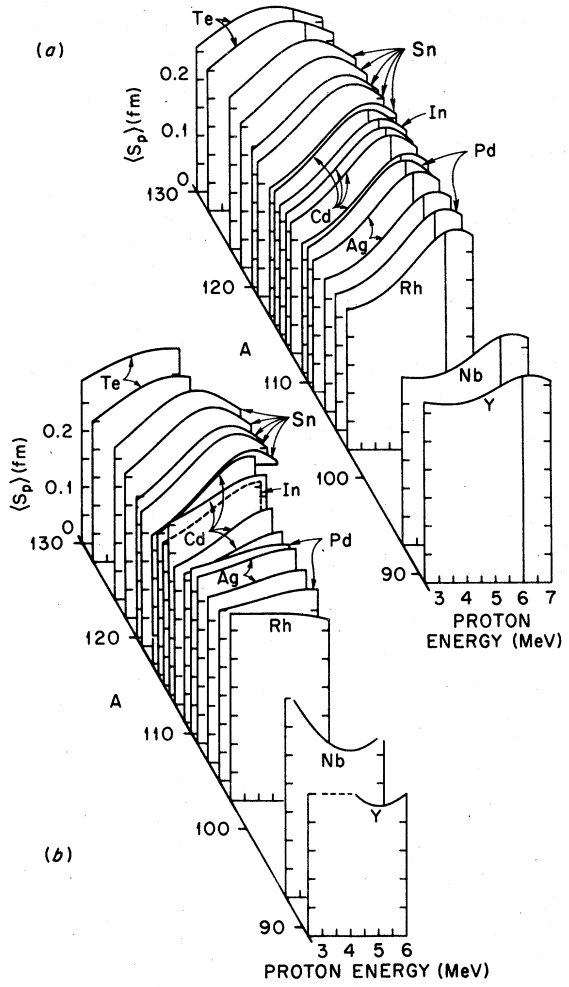

FIG. 1. Excitation functions for reduced proton total reaction cross sections for nuclei from $A = 89$ to 130. (a) Predicted: The required optical model parameters were derived from fits to data on the five Sn isotopes, as shown (see Ref. 3). The vertical lines at 6 MeV aid in visual comparisons to (b). (b) Observed: For clarity of presentation, well fitted curves rather than data are shown. See Sec. IV for enlarged figures of each curve with the data.

cross sections at an average energy, say 5 MeV, agree rather well in both magnitude and shape with the predicted A dependence in Fig. 1(a). However, there was no systematic energy dependence observed such as was found from the precision Sn data and predicted for the other nuclei in Fig. 1(a).

The present work involves an OMP analysis, for which the Sn results[3] form an essential anchor, of cross sections (mostly unpublished) which we measured some time ago. These cross sections are less precise than the Sn data and extend over a smaller energy region, about 3 to 5.8 MeV, which in no case includes the peak of the resonance. Thus each excitation function justifies only two OMP fitting parameters rather than three as in the Sn analysis. Nevertheless, the present data are more accurate than any available in the literature for $89 < A < 130$ and yield new information about the proton OMP.

I. EXPERIMENTS

The data were obtained over a period of several years in Experiments 1 to 4, referenced[2,7-9] in Table I. All were done with the same basic equipment, but the precision improved with time. Thus, Exp. 4 had nearly the quality of the later work[3] on Sn. Protons were accelerated by the 5.5 MV Van de Graaff at Oak Ridge National Laboratory, analyzed by a 90° magnet and collected on the target at the center of Macklin's[10] 4π flat-response neutron detector. Most of the details for Exps. 2–4 are given in the references. The following details concern specific targets, the updating of calibration standards, and details not previously reported for Exp. 1.

A. Neutron detection

There was little error in counting neutrons emitted from the targets. The absolute standard

TABLE I. Experiments, systematic cross section uncertainties not including target uncertainties, and a normalizing factor. The references give partial descriptions of the work reported here.

Experiment	Reference	% Uncertainty for neutrons	% Uncertainty for protons	Normalization
1	Exp. C of Ref. 7	±1.5	±0.6	1.02[a]
2	Exp. 2 of Ref. 2	±0.7	±1.1	1.0[a]
3	Ref. 8	±0.7	±0.6	1.0
4	Ref. 9 and Exp. 3 of Ref. 2	±0.7	±0.6	1.0

[a] Further normalizations for specific targets are discussed in Sec. III.

for the 4π detector in its flat-response region was NBS-II, a National Bureau of Standards RaBe source with a strength, based[3] on measurements from two laboratories,[11] of $1.176\times10^6\pm0.3\%$ neutrons/sec on January 1, 1965. We corrected for the 1620-yr half-life.

The NBS-II was used to establish secondary standards for the (p,n) experiments. About the time of Exp. 1 Gibbons and Macklin[12] used NBS-II to calibrate a local source RaBe-A to $\pm0.5\%$ and an SbBe source to $\pm0.9\%$. Again about five years after Exps. 2–4, Johnson *et al.*[3] obtained NBS-II. Since RaBe-A had been damaged after Exps. 2–4, they made an indirect recalibration using a PuBe source that had been compared to RaBe-A during Exps. 2–4. This recalibration required a correction for the PuBe growth[13] of $0.45\pm0.1\%$ per year (as determined by Bair and Butler[14] from counting the PuBe and another RaBe source over a seven year period). These two calibrations of RaBe-A had relative uncertainties of about $\pm0.7\%$ but agreed to 0.3%. There is little chance of systematic error because this agreement depends on four teams of workers making five intercomparisons of different sources over a period of 20 years.

The three substandards were used in various ways during the (p,n) experiments. Before Exp. 1, Gibbons and Macklin measured the detector's efficiency to $\pm1.5\%$ using RaBe-A; afterwards we measured it to $\pm1.0\%$ using the SbBe source, corrected for its 60.2 ± 0.12 day half-life.[15] The two calibrations agreed to 0.1%. The relatively large $\pm1.5\%$ uncertainty for the first calibration came from the dead time per pulse, 9.5 ± 1.5 μsec. For Exps. 2–4 the deadtime correction was less because the efficiency was reduced from 3% to 0.3% by use of nonenriched BF_3 counters in the 4π detector. During Exps. 2–4 we calibrated twice with RaBe-A and also measured the relative counting rate from the PuBe source, which was used for daily monitoring.

For Exp. 1 we corrected by 6% for absorption in the target holder, as determined from the observed counts from various sources with and without the holder in place. For Exps. 2–4 this correction was reduced to 0.15%. For all experiments we corrected by 0.25% to account for the lower response[10] to neutrons above 1 MeV from the (p,n) reactions. [That is an average value; actually it should be zero near a (p,n) threshold and rise to about 0.5% for 6-MeV protons on a low threshold target.[3]] The various uncertainties are added in quadrature and listed as neutron uncertainties in Table I. The larger value for Exp. 1 arises from the deadtime correction and from $\pm1\%$ uncertainty in target absorption.

B. Proton uncertainties

Each systematic proton uncertainty in Table I is a sum in quadrature of the uncertainty in current integration plus $\pm0.4\%$ propagated[3] to the cross sections from the energy calibrations[16] of the analyzing magnet. The current integrator was calibrated to $\pm0.5\%$, except in Exp. 2 where a mistake resulted in two calibrations with 2% discrepancy. We averaged the two and assigned $\pm1\%$. There were also random errors in setting the proton energies; the corresponding errors in $\sigma_{p,n}$ (included in the error bars in the figures) were[2] $\pm0.7\%$ to $\pm1.3\%$ in Exps. 2–4 and twice as much in Exp. 1.

C. Normalization of experiment 1

The $\sigma_{p,n}$ from Exp. 1 averaged systematically 2% lower than those from the later and more accurate experiments, particularly Exp. 4. Thus, we infer that the correct efficiency for Exp. 1 including target absorption was 2% less than measured. In Sec. III all comparisons between Exp. 1 and Exps. 2–4 are based on Exp. 1 cross sections normalized by 1.02.

D. Targets

Table II lists the targets and several of the properties including the Q values[17] and the areal densities. There are 19 nuclei of which 15 were enriched and used only in Exp. 1. All thin targets were deposited on Pt backings. The enriched targets of Pd, Ag, and Cd were prepared by electrodeposition. All other thin targets were evaporated. Areal densities were computed from the weights measured on a microbalance and from the diameters measured by a microscope. As discussed in Sec. III, some were corrected for nonuniformity. Nominally, the enriched targets were 2.2 cm in diameter (^{125}Te was 3.2 cm) and the natural targets were 1.6 cm.

The largest uncertainties in this work arise from the nonuniformities of the electroplated enriched targets used in Exp. 1. The problems of nonuniformity were further aggravated because the proton beam in Exp. 1 irradiated only the central one-third of the target, rather than two-thirds as in Exps. 2–4. To assess the reliability of the data from Exp. 1 we made further measurements of of two types. Firstly, after Exp. 1 we obtained chemical and/or physical analyses of most of the targets. One test was to scan across a diameter of a target with a collimated x-ray beam and to observe the fluorescent scattering. Secondly, in Exps. 2 and 4 we carefully measured $\sigma_{p,n}$ for the natural elements in order to compare to the weighted sums of isotopic cross sections from

TABLE II. Targets.

Target	Exp.	Enrichment (%)	$-Q$ [a] (keV)	Areal density (mg/cm^2 ± %)	Total systematic uncertainty [b]
^{89}Y	3	100	3618	0.64 ± 2	± 2.2
^{93}Nb	3	100	1189	thick ± 0.3 [c]	± 1.0
^{93}Nb	4	100		thick ± 0.3 [c]	± 1.0
^{103}Rh	1,3	100	1328	1.10 ± 4	± 4.2
^{103}Rh	2	100		thick ± 4 [b]	± 4.2
^{105}Pd	1	78.2	2130	0.83 ± 3	± 3.4
^{106}Pd	1	82.3	3765	0.77 ± 6	± 6.2
^{108}Pd	1	94.7	2703	1.03 ± 10	± 10
^{110}Pd	1	91.4	1661	0.74 ± 3	± 3.4
Pd	2			0.44 ± 5	± 5.2
Pd	4			thick ± 0.3 [c]	± 1.0
^{107}Ag	1	98.8	2199	1.86 ± 2	± 2.6
^{109}Ag	1	99.5	964	1.68 ± 2	± 2.6
Ag	2			2.36 ± 1.5	± 2.0
Ag	4			3.92 ± 1	± 1.4
^{111}Cd	1	89.9	1631	1.10 ± 5	± 5.3
^{112}Cd	1	96.5	3360	1.19 ± 4	± 4.3
^{113}Cd	1	87.3	460	1.82 ± 4	± 4.3
^{114}Cd	1	98.2	2226	2.93 ± 4	± 4.3
^{116}Cd	1	93.8	1246	1.92 ± 4	± 4.3
Cd	2			0.80 ± 3	± 3.3
Cd	4			2.60 ± 0.3	± 1.0
In	2		287 [d]	3.74 ± 1	± 1.6
In	4			3.91 ± 0.3	± 1.0
^{125}Te	1	65.5	959	0.389 ± 3	± 3.4
^{126}Te	1	95.4	2938	0.325 ± 3	± 3.4
^{128}Te	1	96.5	2040	0.798 ± 3	± 3.4
^{130}Te	1	98.2	1233	0.670 ± 3	± 3.4
Te	2			1.045 ± 1	± 1.6

[a] Reference 17.
[b] Quadratic additions of target uncertainties plus uncertainties from Table I.
[c] Uncertainties from stopping powers and energy uncertainties.
[d] Q value for the major (95.5%) isotope ^{115}In.

Exp. 1. Pure and uniform targets of most natural elements are easy to prepare by evaporation because abundant pure supplies of the elements are available. Uncertainties for most of the thin natural targets are discussed in the references for Exps. 2–4. The uncertainties for the thick targets are those propagated from the atomic stopping powers[18] except for Rh, for which the proton energy was not controlled well enough to obtain accurate cross sections from the thick target excitation function. Further details are given in Sec. III.

Light elements are often present as trace contaminants in the targets or on the target backings and defining apertures. Contaminants of B, Cl, and Cu, in particular, give significant backgrounds for low proton energies <3.5 MeV, where the yields from the targets are small. Chlorine is easily detected[7,9] by the sharply rising yield just above the 1.65-MeV ^{37}Cl(p,n) threshold. If Cl(p,n) was detected we subtracted the yield using the excitation function normalized near the threshold. Copper is a common impurity in separated isotopes and in natural Ag. Since the amount of Cu carried over to a target is unpredictable and the yield near the ^{65}Cu(p,n) threshold does not give a "signature" similar to that of ^{37}Cl(p,n), we had the enriched targets (all but Cd) and one natural Ag target analyzed for Cu. We then made corrections using known Cu(p,n) cross sections. We did not obtain similar analyses for the enriched Cd targets but made rough estimates of the possible Cu(p,n) backgrounds by comparison to the natural Cd target, which was free of Cu because it was evaporated at a low temperature. Traces of boron were detected on some of the Pt backings and apertures by the ^{11}B(p,n) yield, a broad bump extending from the threshold at 3.02 MeV to about 4 MeV on an otherwise smooth background. Prior to Exp. 1 we measured the excitation functions for a few Pt blanks and found no ^{11}B(p,n) yield. The enriched targets were deposited on similar back-

ings. Later, prior to Exps. 2–4, we found that some Pt blanks exhibited the $^{11}B(p,n)$ yield. With this knowledge we were able in Exps. 2–4 to minimize this background and to make accurate corrections when necessary. As discussed below, the excitation functions for the enriched targets suggest that some of those backings had traces of boron, even though the tested backings did not.

III. CROSS SECTIONS

Here we present the observed cross sections and further details on individual targets. In order to give linear rather than many-cycle semilog plots, the cross sections are expressed as ratios to smooth empirical excitation functions. Table III lists selected values from the empirical curves and the function for interpolation. The comparisons of the data from the enriched targets with the more accurate data from the natural targets, particularly from Exp. 4, are important. For the subsequent OMP analysis we need data with no more than about ±4% uncertainty. Thus, we omit from the least-squares OMP analyses the results from four targets ^{106,108}Pd and ^{125,126}Te, which have uncertainties of up to about ±10%.

In summary, we have corrected for deadtime losses, for the average lower efficiency for fast neutrons (−0.25%), and for capture in the target holder (−6% in Exp. 1). We have subtracted backgrounds for the room, for the target backing, and for Cl and Cu contaminants in specific targets. As discussed elsewhere[2] we used the observed target-averaged cross section to deduce the $\sigma_{p,n}$ at the average energy in the target. Our results are stated in terms of these discrete values.

In Table II the total systematic uncertainties are additions in quadrature of the proton, neutron, and target uncertainties from I and II. The error bars on the points in the figures represent random errors not including these systematic uncertainties and are combinations in quadrature of the uncertainties from counting statistics, deadtime corrections, random energy fluctuations, and background subtractions. We estimated the background uncertainties to be ±10% of the amount subtracted for the target backing, about ±30% of the Cl(p,n) correction, and ±30% to ±100% for Cu(p,n). For some of the enriched targets the points scatter more than expected from the error bars and this scatter may result from the wandering of the proton beam over the nonuniform target. Thus, part of the systematic errors from Table II could be included in the error bars. Such fluctuations are not reasonably attributed to the actual target-averaged cross section, which should vary smoothly (at least for $A>100$), such as observed for the Sn isotopes.[3] Of course, true variations do occur near isobaric analog resonances (IAR).

A. Yttrium and Indium

Yttrium is ^{89}Y. The ^{89}Y cross sections obtained in Exp. 3 and analyzed in Sec. IV below were reported previously.[8]

Indium is essentially a pure isotope, 95.5%, ^{115}In and 4.5% ^{113}In, and the thresholds[17] are below 2 MeV. The indium cross sections obtained in Exps. 2 and 4 were reported earlier.[2] The two experiments agree on the average to about 0.1%. For simplicity, only the data from Exp. 4 are included in the OMP analysis. We also measured the indium cross sections in Exp. 1. Those values, which are not reported here, showed fluctuations

TABLE III. Smooth (p,n) cross sections in mb. Interpolation between adjacent energies is done using $\exp(-B/E)$ with B determined by the ratio of cross sections at the adjacent energies. Values are listed to three or four figures; however, the uncertainties in the observed $\sigma_{p,n}$ are given by the random error bars in the graphs plus the systematic uncertainties from Table II added in quadrature.

E (MeV)	^{93}Nb	^{103}Rh	^{110}Pd	Ag	^{116}Cd	^{130}Te
2.0	0.0056					
2.25	0.0257					
2.5	0.0918	0.0352	0.0293		0.0132	0.0044
2.75	0.288	0.115	0.0949	0.0333	0.0466	0.0173
3.00	0.762	0.319	0.260	0.162	0.138	0.0556
3.25	1.62	0.772	0.627	0.415	0.357	0.154
3.50	3.12	1.65	1.355	0.950	0.826	0.377
4.00	9.23	5.65	4.91	3.63	3.39	1.68
4.50	21.7	14.8	13.65	10.43	10.54	5.55
5.00	43.3	32.1	31.1	24.9	26.4	14.5
5.50	82.3	60.0	60.2	49.3	54.8	31.5
6.00		100.2	102.4	85.9	96.9	59.3

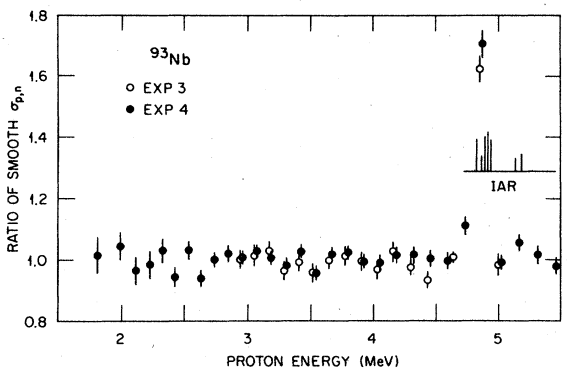

FIG. 2. Cross sections for ^{93}Nb(p,n) determined from a thick target yield. The ordinate is the ratio of $\sigma_{p,n}$ to a smooth curve for which Table III lists representative values and the rules of interpolation. The insert shows the known positions and relative heights of IAR's (see Ref. 19).

of a few percent but agreed on the average to 1% with the accurate data of Exps. 2–4.

B. Niobium

Niobium is ^{93}Nb. Figure 2 shows the $\sigma_{p,n}$ deduced from thick target yields from Exps. 3 and 4. No evidence was found for target contaminants. The data from the two experiments agree on the average to 1.4%, which is consistent within the error bars. The enhanced yields near 5 MeV are due to IAR; the insert shows the known[19] energies and approximate relative magnitudes of the resonance cross sections.

C. Rhodium

Rhodium is ^{103}Rh. Figure 3 includes the $\sigma_{p,n}$ obtained using the same thin target in both Exps.

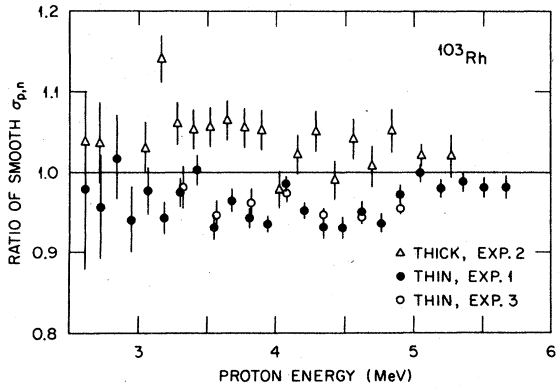

FIG. 3. Ratios to a smooth curve (Table III) of $\sigma_{p,n}$ for ^{103}Rh measured both for a 1.10 mg/cm^2 target and by differentiating a thick target yield. The averages for the two targets disagree by 8%; each is normalized by 4% for the subsequent OMP analysis.

1 and 3. The two experiments agree on the average to 0.3%. Corrections were made for Cl(p,n). On the basis of subsequent x-ray scans we assumed the central areal density to be 2.3% less than the overall average deduced from the total weight and area. The figure shows also the $\sigma_{p,n}$ deduced from the thick target yield in Exp. 2. The thick and thin excitation functions disagree on the average by 8%. In assessing this disagreement we note that Exp. 2 did not achieve the energy control required for thick targets. (Other cross sections obtained from thick targets in Exp. 2 were later found to be as much as 5% too high.) But we also lack confidence in the nonuniform thin target. Therefore, for the subsequent OMP analysis, we give equal importance to the two targets by normalizing the thick and thin values by 0.96 and 1.04, respectively. The systematic uncertainties of ±4% in Table II are assigned on this basis. The agreement in shape of the excitation functions is more significant for the OMP analysis than the uncertainty in magnitude.

D. Silver

Since Ag has only two isotopes with nearly equal abundances, the isotopic cross sections can be deduced from relatively poor data from enriched targets supplemented by accurate measurements on natural Ag. Figure 4(a) shows the accurate data from Exp. 4 for natural Ag. No Cl(p,n) background was detected and the comparison below with Exp. 2 shows that the Cu(p,n) background was negligible. We measured the average areal density to ±0.3% by weighing. This accuracy was confirmed by the observed average 0.5% agreement with the thick target data from Exp. 4. Nevertheless, in Table II we assign ±1% uncertainty because the thick-thin comparisons showed anomalous fluctuations. In particular, the two points above 5.5 MeV may be 1% low.

Figure 4(a) also shows the natural Ag from Exp. 2. No Cl(p,n) background was observed but an analysis showed 0.1% Cu. The Cu(p,n) subtraction was 2.5% at 3 MeV but less at higher energies. The excellent agreement of $\sigma_{p,n}$ with Exp. 4 represents a normalization of about 1% because we chose the target density for Exp. 2 from several discrepant values. The density used was reported to us from a quantitative emission flame spectroscopic analysis of a central target cutout including the bombarded area. But the densities deduced earlier by weighing the original target and the cutout were, respectively, 2.6% and 1.3% higher.

Figure 4(b) shows the ^{107,109}Ag cross sections from Exp. 1. The background corrections included Cl(p,n) and Cu(p,n), the latter deduced from

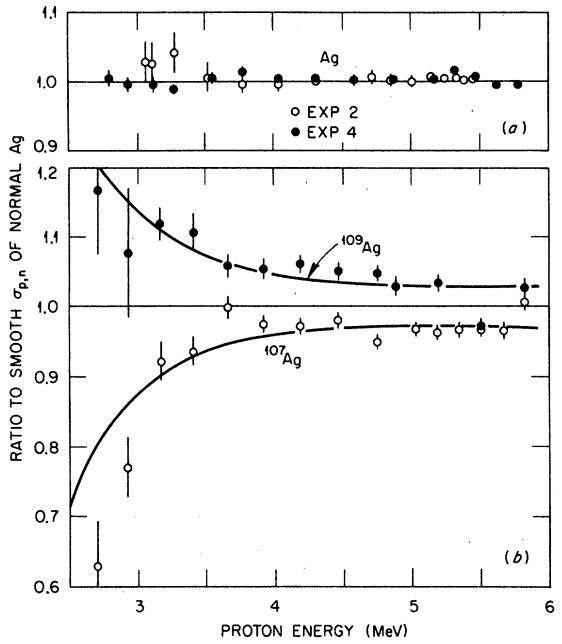

FIG. 4. Ratios to a smooth curve (Table III) of $\sigma_{p,n}$ measured (a) for natural Ag and (b) for ^{107,109}Ag. The curves in (b) are drawn visually to fit the data with the restrictions that ^{107}Ag must go to zero at the (p,n) threshold and the isotopically weighted sum must be unity to agree with the more accurate data in (a) for natural Ag.

the analyzed 0.2 and 0.05 atomic percent of Cu in ^{107}Ag and ^{109}Ag. We submitted cutouts of these targets for flame analysis along with the natural Ag above. In two independent sets of flame analyses the relative values for the three targets were reproduced to ±1%. We used the relative values to deduce the ^{107,109}Ag densities on the same basis as for the natural Ag. Originally we found 5 to 7% higher densities by weighing the full enriched targets. The discrepancy is attributed to the targets being thinner than average in their central regions.

The smooth curves in Fig. 4(b) are drawn visually to fit the data under the necessary conditions that the isotopically weighted sum of the curves is unity and the ^{107}Ag curve goes to zero at the 2.22-MeV threshold. Smooth excitation functions are expected in this energy region, which includes[20] no IAR's. We attribute the deviations from the curves to target nonuniformities and, at low energies, to possible errors in background corrections. The data points used for the following OMP analysis are obtained by multiplying the accurate Ag data from Fig. 4(a) by the curves in Fig. 4(b).

E. Palladium

Figure 5 includes the accurate $\sigma_{p,n}$ obtained in Exp. 4 from a thick natural Pd target. Since Pd has several isotopes these results reveal little about the individual isotopes but do provide an overall normalization for the less accurate data from the enriched targets.

Figure 5 includes also data from the thin Pd target of Exp. 2. The large error bars at low energies arise from the Cl(p,n) subtraction. A spectroscopic analysis showed no other impurities. We weighed a central two-third cutout of the target before and after the Pd was removed by acid and found the central density to be 5% more than the average for the whole target. This discrepancy indicates a nonuniformity, as did also the poor reproducibility (±3%) of some points. The central density would seem to be correct because we bombarded the cutout area, but we used the average for the entire target to normalize to the more accurate data from Exp. 4. These data from Exp. 2 are included to confirm the shape of the excitation function.

Figure 5 includes the isotopically weighted sums of the ^{105,106,108,110}Pd cross sections that were obtained in Exp. 1 and are discussed below. The isotopic cross sections for each point were measured at slightly different energies, depending on

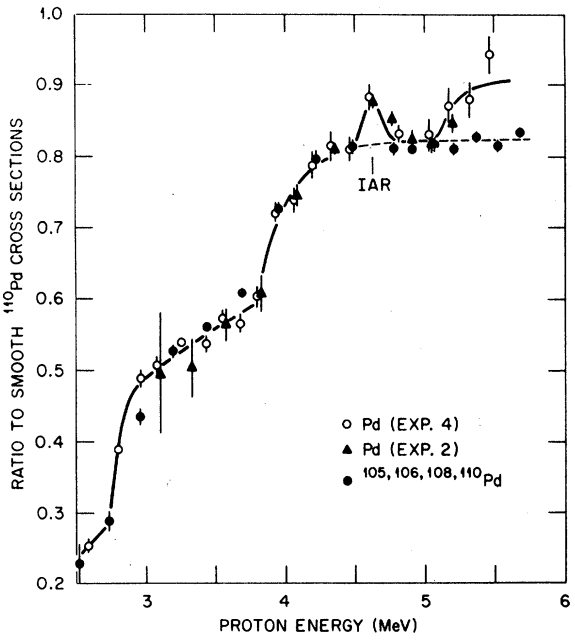

FIG. 5. Ratios to a smooth curve (Table III) of $\sigma_{p,n}$ for natural Pd. A thick target was used for Exp. 4 and a thin target, reasonably normalized, for Exp. 2. The solid curve is drawn visually to fit the data, with breaks at the ^{108,106,104}Pd(p,n) thresholds. The IAR corresponds to the dashed IAR for ^{105}Pd in Fig. 6. The solid circles denote isotopically weighted sums of the ratios from Fig. 6 and do not include the ^{104}Pd yield above the 5.08-MeV threshold.

the target thickness, but the summations were made easily using the ratios to the smooth curve. We weighed central cutouts of these targets just as for Pd in Exp. 2 and assumed the central densities to be correct in order to obtain agreement with Exp. 4. For ^{105}Pd and ^{110}Pd the average densities were the same as the central densities; those targets must have been uniform and are listed in Table II with small uncertainties. For ^{106}Pd and ^{108}Pd, respectively, the central densities were 8% and 15% below the averages; those targets must have been nonuniform and are listed with larger uncertainties.

The smooth solid curve in Fig. 5 is drawn visually with breaks at the thresholds for ^{108,106,104}Pd. Above 5 MeV the weighted sums lies below natural Pd because ^{104}Pd is excluded. As discussed below, the peak near 4.6 MeV is attributed to an IAR in ^{105}Pd + p. The less accurate data from Exp. 2 were included primarily to show that this peak is real.

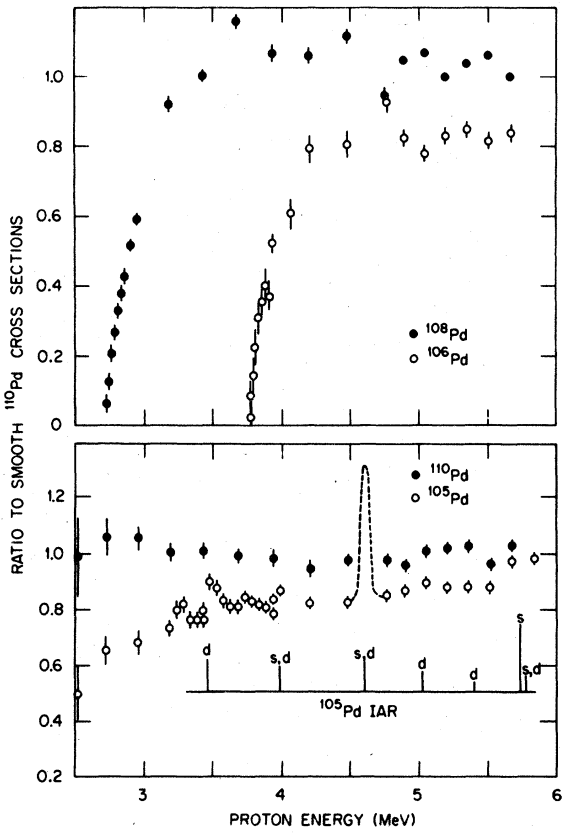

FIG. 6. Ratios to a smooth curve (Table III) of $\sigma_{p,n}$ for Pd isotopes. The expected positions and relative magnitudes of the IAR's are indicated (see text). The dashed curve for ^{105}Pd is an IAR deduced from the cross sections for natural Pd in Fig 5. The fluctuations of some points for ^{106,108}Pd are attributed to target nonuniformities, not to IAR's.

Figure 6 shows the individual ^{105,106,108,110}Pd cross sections deduced using the central target densities discussed above. We have made self-consistent corrections for the minor isotopes in each target. For ^{104}Pd, which was only 3.8% of the ^{105}Pd target and less for the others, we assumed consistent cross sections. Backgrounds included Cl(p,n) and Cu(p,n). Spectroscopic and chemical analyses showed the ^{105}Pd, ^{106}Pd, ^{108}Pd, and ^{110}Pd targets to have 0.15, 1.5, 0.0, and 0.15% of Cu, respectively. We attribute the fluctuations for ^{106}Pd and ^{108}Pd to the nonuniformities of these targets. Since these two targets have large uncertainties and ^{106}Pd has a high threshold, they are omitted from the subsequent OMP analysis.

Several IAR are expected for ^{105}Pd(p,n). Figure 6 shows the positions for the stronger resonances, including multiplets, predicted from the neutron analogs found[21] by ^{105}Pd(d,p). The energies are based on a typical[20] 13.00-MeV Coulomb displacement energy, and the magnitudes of the resonance cross sections are calculated with weighting based on spectroscopic terms and on optical model transmission factors.[8,21,22] These magnitudes agree qualitatively with the observed fluctuations. A strong resonance (dashed curve) is probable for the 4.616-MeV s-d multiplet because a pronounced peak was observed for natural Pd in Fig. 5, even though ^{105}Pd is only a 22% isotope.

F. Cadmium

Since Cd has a low melting point we started each bombardment with a small current at a high energy and took care to avoid beam damage subsequently at lower energies. For Cd, as for Pd, the data from Exp. 4 provide an accurate standard. Figure 7(a) includes the accurate $\sigma_{p,n}$ for natural Cd from Exp. 4 and the less accurate values from Exp. 2, normalized by +3% to give average agreement with Exp. 4. The energies[23] for the ^{111,113}Cd ground state IAR are indicated and the solid curve is drawn visually to fit the nonresonance cross sections. Breaks in the curve are shown at the ^{112}Cd and ^{110}Cd thresholds[17] of 3.39 and 4.76 MeV, respectively. The target thicknesses and proton energies were such that the IAR were missed in Exp. 2 but averaged over in Exp. 4. Thus, for Exp. 4 the two points near the IAR lie above the smooth curve.

Figure 7(a) also shows the weighted sums of the ^{111,112,113,114,116}Cd cross sections discussed below. Above the 3.4-MeV threshold for ^{112}Cd the agreement with Exp. 4 confirms that the isotopic cross sections are correct on the average. Above 4.76 MeV the summed points are low because ^{110}Cd(p,n) is excluded. Below 3.4 MeV the sums are too high. One might think that this discrepancy arises

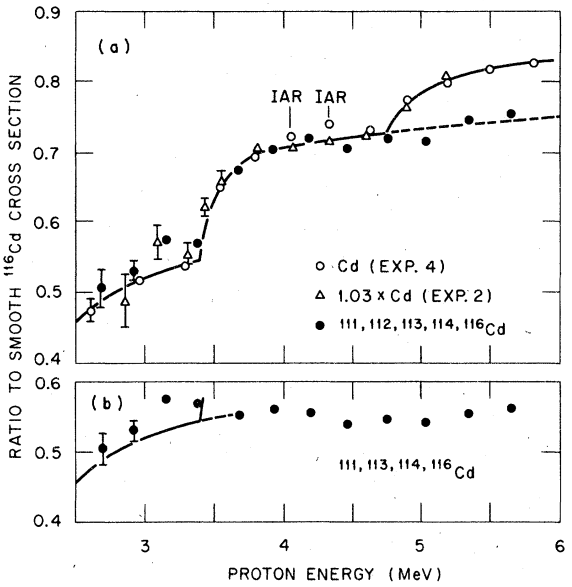

FIG 7. (a) Ratios to a smooth curve (Table III) of $\sigma_{p,n}$ for natural Cd. The data from Exp. 2 are normalized to give average agreement with Exp. 4. The positions of the IAR's in ^{111,113}Cd are indicated (see Ref. 23). The solid curve is drawn visually to fit the data, with breaks at the ^{112,110}Cd thresholds. The solid points are isotopically weighted sums of the data from Fig. 8 and do not include ^{110}Cd. (b) The isotopically weighted sums with both ^{110}Cd and ^{112}Cd excluded. The solid curve is the same as in (a), and the discrepancies of the points from the curve are attributed to a contaminant ^{11}B(p,n) reaction.

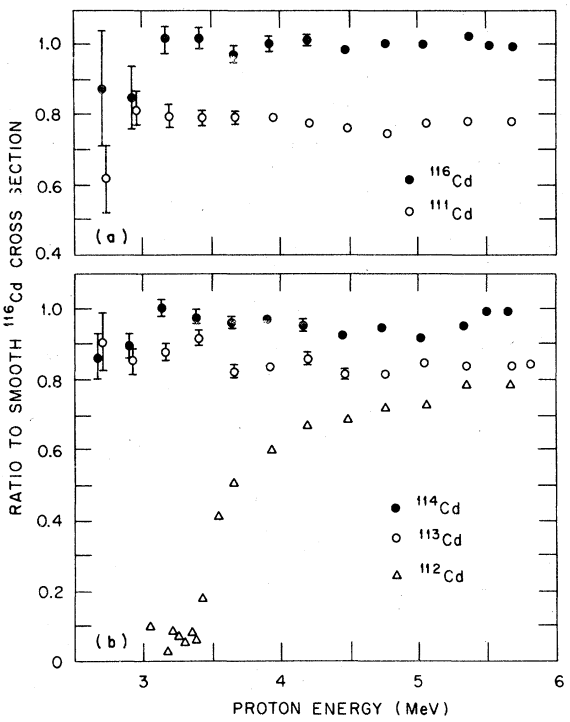

FIG. 8 Ratios to a smooth curve (Table III) of $\sigma_{p,n}$ for isotopes of Cd. The yield below the ^{112}Cd(p,n) threshold is attributed to a contaminant reaction, probably ^{11}B(p,n). Similar contaminant yields may be present near 3.2 MeV for the other isotopes. These contaminant ratios decrease above 3.5 MeV.

from errors in isotopic target thicknesses, i.e., the partial sum for ^{111,113,114,116}Cd could be too high and the values for ^{112}Cd could be too low such that the total above the ^{112}Cd threshold would still be correct. But Fig. 7(b), which shows the partial sum, demonstrates that the high points are on a local maximum. As discussed below we attribute this to backgrounds of Cu(p,n) and/or B(p,n) in the targets or backings.

Figure 8 shows the ^{111,112,113,114,116}Cd cross sections from Exp. 1. We have made self-consistent corrections for the minor isotopes in each target. For ^{110}Cd, which was 1.7% of ^{111}Cd, we assumed a reasonable excitation function. A Cl(p,n) background was subtracted for each target. For ^{112}Cd, which has a high threshold, we also subtracted Cu(p,n) normalized to the spurious yield observed below 3 MeV. The correction corresponded to 0.2 atomic percent Cu or, in terms of the ordinate in Fig. 8, to ratios of 0.10, 0.03, 0.01, and 0.004, respectively, at 3.0, 3.5, 4.0, and 5.5 MeV. Unfortunately, we did not obtain Cu analyses for the other targets and so made no correction. As suggested from Fig. 7(b), one or more of the other targets has a significant Cu(p,n) and/or B(p,n) backgrounds for energies below 3.5 MeV.

We assumed the enriched targets to be uniform. The small fluctuations of the points support this assumption. (The points for ^{111,113}Cd miss the IAR's.) Some time after Exp. 1 we made central one-third cutouts for the ^{112,113,116}Cd targets (^{111,114}Cd were no longer available) and compared the central and average weights of the deposits. The results suggest that the ^{112}Cd, ^{113}Cd, and ^{116}Cd cross sections should be changed by +3.5, −3.5, and −2.5%; respectively. We have simply assigned ±4% uncertainty to each target in Table II except ^{111}Cd; the ^{111}Cd target is assigned ±5% because it had an irregular perimeter.

G. Tellurium

Figure 9 shows the $\sigma_{p,n}$ for natural Te from Exp. 2. The target was evaporated at a low temperature to avoid Cu contamination and the areal density was determined to ±1% from the weight and area. No Cl(p,n) background was observed; however, the subtracted background included a B(p,n) yield equal to that observed in Exp. 2 from other backings prepared exactly as that for the

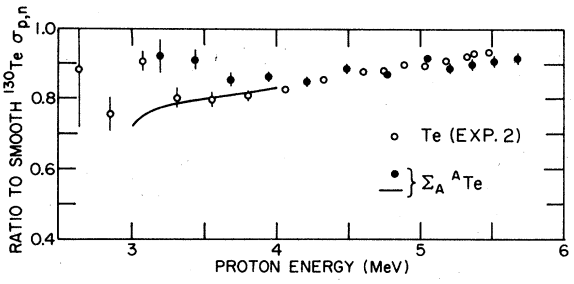

FIG. 9. Ratios to a smooth curve (Table III) for $\sigma_{p,n}$ of natural Te and the isotopically weighted sum of ratios from Fig. 10. The sums include estimates of the minor ^{120,122,124}Te yields. The smooth curve is the sum based on smooth curves from Fig. 10. The anomalous point near 3.1 MeV for natural Te is attributed to a contaminant ^{11}B(p,n) reaction.

target. The anomalously high point at 3.08 MeV was reproducible. This may mean that the boron was on the apertures before the target rather than on the backing. [The large detector made it difficult to localize the B(p,n) source.] If so, the proton energy used for calculating the B(p,n) background should not have been reduced by the 50-keV loss in the target; this would lower the point at 3.08 MeV because it is near the ^{11}B(p,n) threshold (3.02 MeV) where the yield rises rapidly. Other points have little error from this possible effect.

Figure 10 shows the enriched Te cross sections measured in Exp. 1. Here again we have made self-consistent corrections for the minor isotopes in each target. Later x-ray scans of the targets showed them to be uniform to ±2%. The ±3% uncertainties in Table III are estimated from the weights, areas, and possible nonuniformities. The backgrounds were relatively large, partly because the cross sections are small for these high-Z targets and partly because the targets, particularly ^{125,126}Te, were too thin to give good ratios of yield to background at the lower energies. Backgrounds included Cl(p,n) and Cu(p,n). An analysis showed 0.02 to 0.04 atomic percentage of Cu for ^{125,126,130}Te but 0.85% for ^{128}Te. Since 0.85% of Cu was too large to be consistent with the observed yield, we ignored this value and assumed 0.14% to make the point at 2.96 MeV consistent with higher energies. The error bars in Fig. 10 are large because of the backgrounds; they include the full Cu subtraction for ^{128}Te and half the subtraction for the others.

Above 4 MeV in Fig. 10, where the background corrections and threshold effects are relatively small, the systematic trend of the isotropic cross sections is reasonable; the relative values averaged over energy are 0.77, 0.87, 0.91, and 1.00 for ^{125,126,128,130}Te. For ^{125}Te a yield might have been expected from the IAR[24] but the proton energies of 4.907 and 5.057 MeV used for this thin target apparently missed the resonance. Returning to Fig. 9, we find above 4 MeV that the weighted sums of isotopic cross sections agree on the average to <1% with natural Te. For the contribution of the unmeasured minor isotopes to the sums, we have used the curves from Fig. 10 for ^{122}Te (2.5%) and ^{124}Te (4.6%) and assumed 0.7 of ^{130}Te(p,n) for ^{123}Te (0.9%).

Below 4 MeV the summed points rise above natural Te. The solid curve, which agrees with natural Te, is an isotopically weighted sum of the curves shown in Fig. 10 below 4 MeV. Of these curves the one for ^{126}Te is drawn consistently with other thresholds; those for the other isotopes are visual extrapolations from above 4 MeV. We attribute the discrepancies between the curves and the data to B(p,n) backgrounds from the enriched target backings, even though the sample backings tested in Exp. 1 showed no B(p,n). These comparisons establish a confidence level for these data.

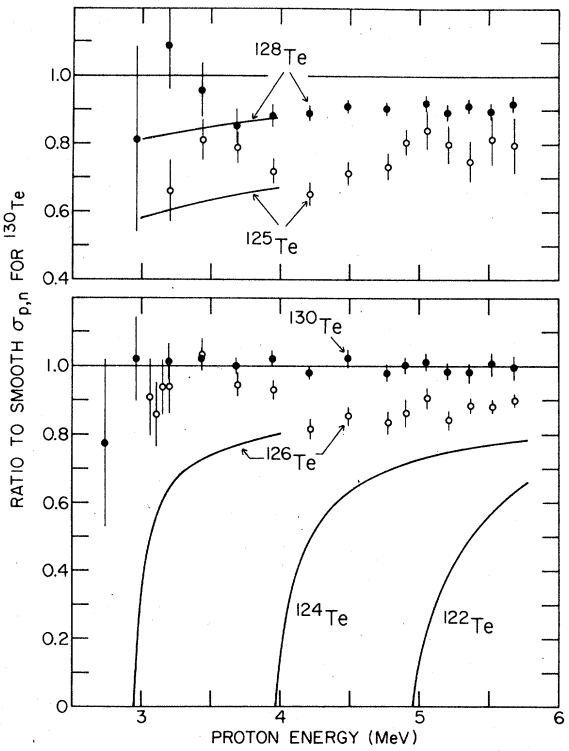

FIG. 10. Ratios to a smooth curve (Table III) of $\sigma_{p,n}$ for isotopes of Te. The ^{122,124,126}Te curves are drawn to rise from the thresholds with shapes analogous to curves for Sn isotopes (see Ref. 3). The curves for ^{125,128}Te are drawn consistently with the yields above 4 MeV and with natural Te. The discrepancies of some points from these curves are attributed to ^{11}B(p,n) from a trace contaminant.

For the subsequent least-squares OMP analysis we omit points below 3.5 MeV for ^{128}Te. We also omit entirely the data for the very thin targets ^{125,126}Te, because the poor yield-to-background ratios resulted in large fluctuations even at higher energies.

IV. ANALYSIS

A. Optical model potential form

We use a conventional proton OMP for calculating proton total reaction cross sections. It is a sum of Woods-Saxon, surface absorptive, spin-orbit, and Coulomb potentials:

$$V(r) = -V_R f(r,R_R,a_R) + i4a_D W_D \frac{d}{dr} f(r,R_D,a_D) + V_{so} \frac{\vec{\sigma}\cdot\vec{l}}{r} \left(\frac{\hbar}{m_\pi c}\right)^2 \frac{d}{dr} f(r,R_{so},a_{so}) + V_c(R_c) , \quad (1)$$

where

$$f(r,R,a) = \left[1 + \exp\left(\frac{r-R}{a}\right)\right]^{-1} ,$$

$$R_x = r_x A^{1/3} ,$$

and

$$V_R(E) = V_R(0) - b_0 E .$$

As discussed in Sec. IV E we fix all but two of the eleven parameters.

B. Corrections for γ-ray and proton emission

At the higher proton energies the compound nucleus decays mostly by neutron emission. Thus, an observed cross section $\langle\sigma_{p,n}\rangle$ averaged over the many levels of the compound nucleus is essentially the reaction cross section $\langle\sigma_r\rangle$ for the average potential model. But at energies nearer to the (p,n) threshold the emission of γ-rays is important. Proton re-emission may also compete, especially for the lighter nuclei ^{89}Y and ^{93}Nb.

Using Penny's[3,26] computer code HELGA to make Hauser-Feshbach[25] statistical theory calculations, as reviewed in Sec. VI A–E of the Sn paper,[3] we predict an $F(E)$ for each nucleus:

$$F(E) = \langle\sigma_{p,n}\rangle / \langle\sigma_r\rangle . \quad (2)$$

This ratio vanishes at the (p,n) threshold and approaches unity at the higher energies, which are still well below the Coulomb barrier.

The predictions of $F(E)$ require data from several sources. We need the proton and neutron OMP, the γ-ray strength function, the Fermi-gas density parameter, and the low-lying levels for the target, compound, and final nuclei. To obtain the proton OMP we use an iterative procedure such that the parameters used to calculate $F(E)$ are consistent with the values required for the subsequent analysis of the (p,n) cross sections. [Actually, the proton OMP is not very critical for obtaining $F(E)$.] For the neutron OMP we use the parameters which Moldauer[27] deduced from low energy neutron data for $30 < A < 140$. The neutron spin-orbit term is not critical and is omitted for computational convenience. The γ-ray strength functions were obtained[28] by fitting average radiative widths in the present mass region. Low-lying levels are obtained from the Nuclear Data Sheets[29-39] supplemented by recent references.[40-44] For the Fermi-gas constant we assume the average curve deduced[28] from earlier fittings[45,46] of level densities in this mass region. Finally, we deduce[28] for each nucleus a second density parameter, the fictitious ground state Δ, consistent with the low-lying states.

The fluctuation[47] factor θ which enters[3] into $F(E)$ is based on a Porter-Thomas distribution (χ^2 with one degree of freedom) of the partial proton or neutron widths for emission to each final state. For γ rays the calculations involve the total width for emission to all final states; these widths have a narrow distribution which we approximate by χ^2 with infinite degrees of freedom. The factor θ is less than unity near the (p,n) threshold where few neutron channels are open and approaches unity at higher energies.

C. Corrected analyses for the Sn isotopes

Although the statistical model equations in Sec. VI A–D of Ref. 3 are correct, there was an error in the computer code such that the fluctuation factor θ was always set equal to unity. Thus, the predictions in Sec. VI E of Ref. 3 show $F(E)$ increasing too rapidly above each (p,n) threshold. Johnson *et al.*[3] concluded erroneously that the statistical model was a partial failure and compensated by introducing two additional free parameters into their OMP analysis of the six Sn isotopes. Using a corrected code[26] with statistical model parameters deduced as outlined above we have recalculated $F(E)$ and repeated individual optical model analyses of the published data[3] on ^{117,119,120,122,124}Sn. [We omitted ^{118}Sn because the high threshold makes the OMP parameters too sensitive to $F(E)$.] The points in Fig. 11 show the least-squares fitted OMP parameters, $V_R(0)$, W_D, and a_D, and the straight lines are from the earlier analysis.

D. Definition of the reduced cross sections

In the following analysis OMP parameters are chosen by least squares to fit the observed $\sigma_{p,n}$ corrected for γ-ray and proton emission. To in-

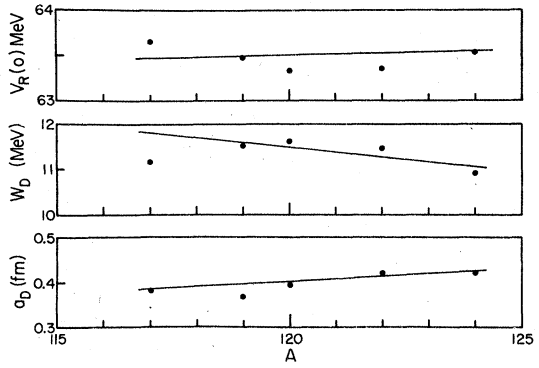

FIG. 11. Corrected OMP analysis of the ^{117,119,120,122,124}Sn(p,n) cross sections from Ref. 3. The points are the best fit parameters. The lines are fits obtained in Ref. 3 by adjusting two *ad hoc* parameters introduced to compensate for an error in the statistical model code that was not recognized by the authors. The agreement of the points and lines show that the OMP results of Ref. 3 were correct even though some of the conclusions regarding the statistical model were wrong.

terpret a fitted OMP it is instructive not only to give the parameters but also to show excitation functions. To avoid a many-cycle semilog plot which would obscure the details, we divide out the Coulomb effects and plot both data and theory linearly. This procedure is analogous to the familiar one of plotting proton differential cross sections relative to Rutherford scattering.

To deduce a reasonable divisor for the Coulomb effects we first write the reaction cross section for l-wave protons,

$$\langle\sigma_r\rangle_l = (2l+1)\pi k^{-2} T_l , \tag{3}$$

where T_l is the transmission factor. (Spin-orbit splitting is neglected here for simplicity of illustration but included in the final analyses below.) Figure 12 shows T_l calculated for p waves for ^{124}Sn + p using the real well and the imaginary well geometry deduced from the observed cross sections[3] but various imaginary well depths from 0.5 to 12 MeV. The resonance for $W_D = 0.5$ MeV results from the $3p$ state, which is quasibound by the combined nuclear-Coulomb potential. As W_D increases, this resonance broadens such that for $W_D = 12$ MeV, which is about the value required to fit the observed $\sigma_{p,n}$, the resonance is no longer apparent.

Our task is to divide out the dominant exterior Coulomb effects in order to reveal the broadened nuclear resonance for large W_D. If we had measured $\sigma_{p,n}$ for each partial wave and if the nuclear potential were a square well we could plot $T_l/(4\pi P_l)$, where P_l is the penetrability kR/A_l^2 at the square-well radius and k is the proton wave number. [For small T_l the ratio $T_l/(4\pi P_l)$ is the nuclear strength function or reduced width per energy interval.] The corresponding radius for a diffuse-edge potential is not well defined; nevertheless, we can reveal qualitative features by using an appropriate radius. Figure 13 shows $T_l/(4\pi P_l)$ for p waves calculated from Figure 12 for $R = 1.45\ A^{1/3}$. We see that most of the Coulomb dependences have been removed such that the peak energy remains nearly fixed as the resonance broadens. Since the energy of the peak would have been increased or decreased if the radius had been chosen respectively larger or smaller, the location of the resonance for large W_D is not given precisely by this simple analysis. Nevertheless, it is clear that the broadened resonance results from the $3p$ state.

The actual measurements sum over partial waves. For consistency with the Sn analysis[3] and with earlier literature[2,5] we plot a reduced cross section defined by

$$\langle S_p\rangle = R\,\frac{\langle\sigma_r\rangle}{4\pi^2 k^{-2}\sum_l (2l+1)P_l} , \tag{4}$$

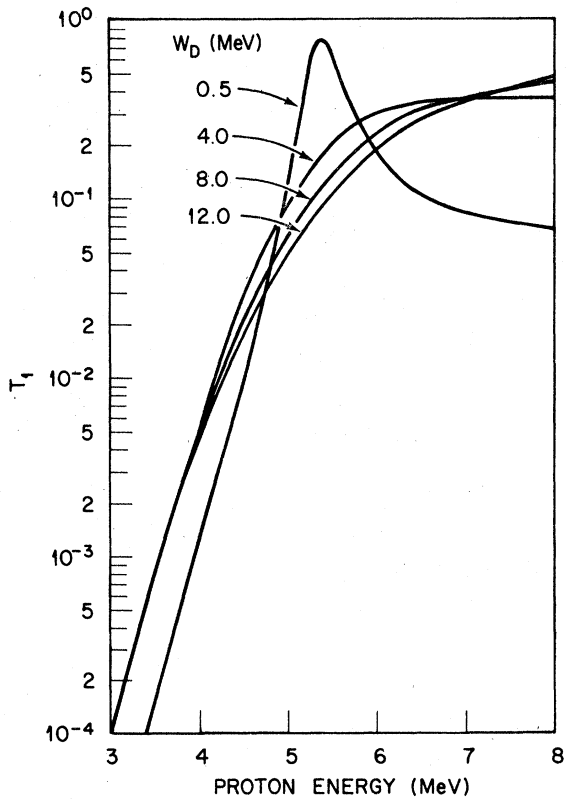

FIG. 12. p-wave transmission factors calculated for the fitted OMP for ^{124}Sn + p except for variations in the imaginary well depth. The resonance results from the quasibound $3p$ state.

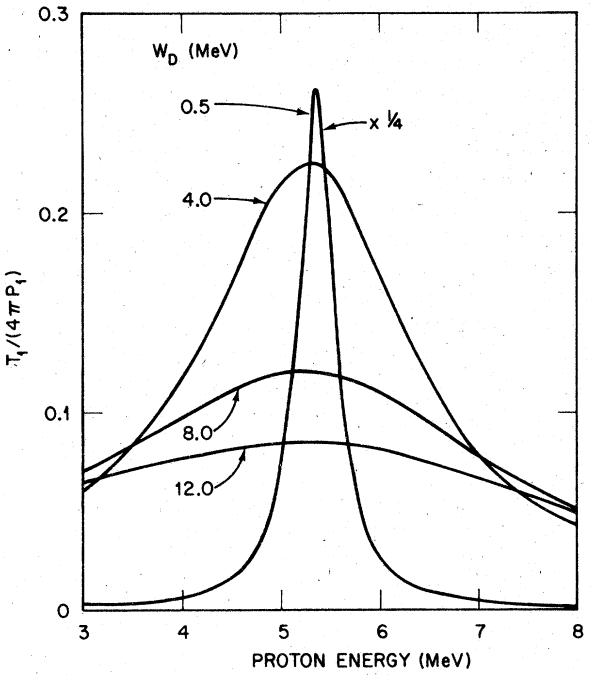

FIG. 13. p-wave transmission factors from Fig. 12 divided by 4π times penetrabilities calculated at 1.45 $\times A^{1/3}$ fm.

where P_l is calculated at 1.45 $A^{1/3}$ fm, the same radius as used in Fig. 13. The divisor is seen to be a weighted sum of $4\pi P_l$. By analogy, $\langle S_{p,n}\rangle$ is found by replacing $\langle\sigma_r\rangle$ by $\langle\sigma_{p,n}\rangle$. Figure 1(a) shows curves of $\langle S_p\rangle$; each broad maximum is attributed to the $3p$ state. Further discussions of Eq. (4) appear in the literature.[2,5]

E. Fixed and variable OMP parameters

The previous analysis[3] of the precision Sn(p,n) cross sections is an essential anchor for the present work. Each Sn isotope required only three free OMP parameters to fit the energy, width, and height of the observed resonance in $\langle S_p\rangle$, and a study of parameter space showed that a_D, W_D, and $V_R(0)$ were appropriate parameters. These were adjusted by least squares while the other eight were fixed according to published analyses of data obtained above the barrier. Table IV lists the fixed values. (The small isotopic dependence of r_c is neglected here, and the value listed is for ^{117}Sn.)

We use the same fixed parameters but must fix one more because only two free parameters are needed to fit the magnitude and energy dependence of $\langle S_p\rangle$ for each target over the energy range of our work. Our choice is to fix $V_R(0)$ for all isotopes of each element at the value listed in Table V. These values were calculated for the isotope in the valley of β stability using a conventional[48] isospin and Coulomb dependence,

$$V_R(0) = V_0 + 24(N-Z)/A + 0.45\,Z/A^{1/3}, \qquad (5)$$

where $V_0 = 55.4$ MeV has been chosen to fit $V_R(0)$ for the Sn isotope in the valley of β stability.

The remaining free parameters are W_D and a_D. Qualitatively, for our mass and energy region, the imaginary well depth W_D controls the energy dependence, and the diffuseness a_D varies the magnitude of $\langle S_p\rangle$. Since the following analysis of the data shows that W_D is an essential variable whereas a_D comes out nearly constant, the fixed and free roles of $V_R(0)$ and a_D could possibly have been reversed for most of the targets. In fact, the fits for ^{89}Y and ^{93}Nb require that $V_R(0)$ be free whereas a_D can be fixed.

TABLE V. Fixed real well depths.

Element	$V_R(0)$ (MeV)	Element	$V_R(0)$ (MeV)
Y	62.3[a]	Ag	62.9
Nb	62.3[b]	Cd	63.1
Rh	62.7	In	63.4
Pd	62.9	Te	64.0

[a] In the final analysis adjusted by least squares to 61.5 MeV.
[b] In the final analysis adjusted by least squares to 61.1 MeV.

F. Least-squares OMP analysis

The (p,n) cross sections were fitted by least squares using the OMP program GENOA[49] modified to include the statistical model predictions of the ratio $F(E) = \langle\sigma_{p,n}\rangle/\langle\sigma_r\rangle$. Figures 14 and 15 list the best fit parameters and show the fitted curves (lower solid) and data in terms of $\langle S_{p,n}\rangle$ for 14 nuclei. The corresponding $\langle S_p\rangle$ are shown by the upper solid curves and are reproduced in Fig. 1(b) of the Introduction. Data shown by triangles

TABLE IV. Fixed proton optical-model parameters.

V_{so} (MeV)	r_{so} (fm)	a_{so} (fm)	r_R (fm)	a_R (fm)	b_0 (MeV^{-1})	r_D (fm)	r_c (fm)
6.4	1.03	0.63	1.2	0.73	0.32	1.3	1.22

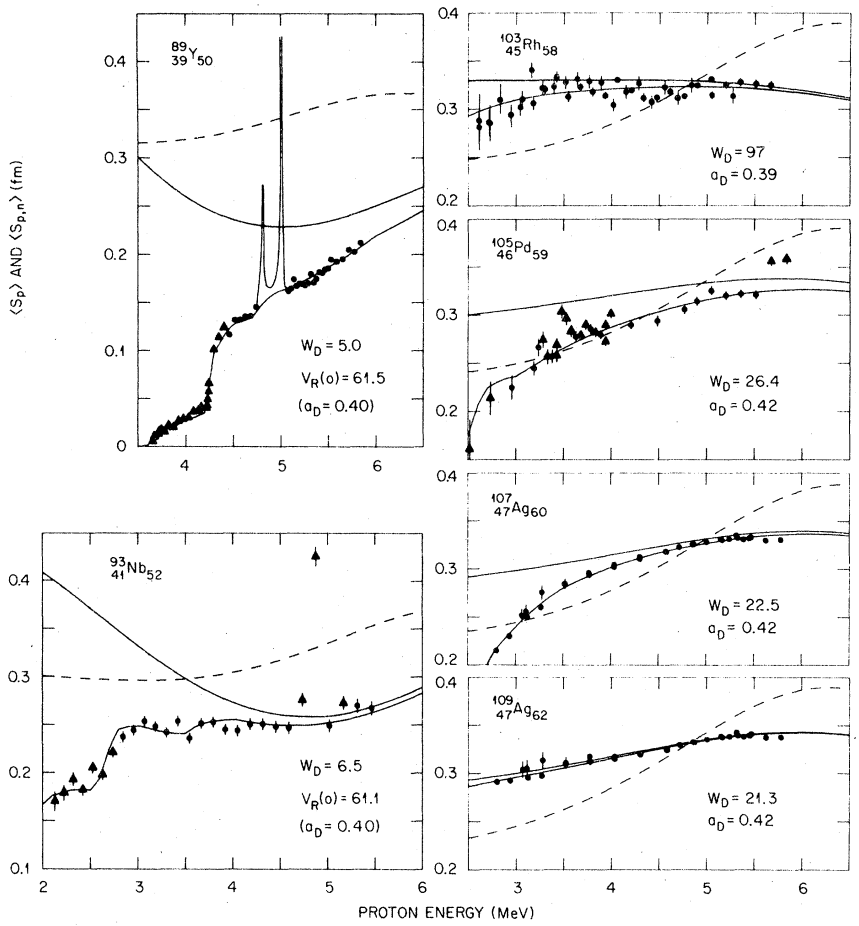

FIG. 14. Reduced (p,n) and total reaction cross sections, $\langle S_{p,n}\rangle$ and $\langle S_p\rangle$. In each figure the data points and the lower solid curve are $\langle S_{p,n}\rangle$. The upper solid curve shows the corresponding $\langle S_p\rangle$. The best fit parameters are listed and the fixed parameters are from Tables IV and V, except that a_D was fixed as indicated for ^{89}Y and ^{93}Nb. Data shown by triangles were omitted from the search. The dashed curve is $\langle S_p\rangle$ predicted on the basis of the Sn analyses using $W_D = 11.8$ MeV, $a_D = 0.385$ fm, and the fixed parameters in Tables IV and V.

were omitted from the fit because they are either too near the IAR's (^{93}Nb and ^{105}Pd), or too near the (p,n) threshold for a reliable prediction of $F(E)$, or too low in energy for reliable background subtraction. Actually, except for points near the IAR's, the fitted curves usually agree well with the omitted points. The dashed curves are $\langle S_p\rangle$ predicted with the imaginary part of the potential taken from the Sn analysis (specifically $a_D = 0.385$ fm and $W_D = 11.8$ MeV for ^{117}Sn) and the fixed parameters from Tables IV and V. These latter curves are reproduced in Fig. 1(a).

Figure 16 shows the imaginary diffuseness a_D for $A > 100$, including the values for the Sn isotopes from Fig. 11. The values average about 0.4 fm with little fluctuation. Since a_D acts partially as a normalizing factor, some of the fluctuations may result from errors in target thicknesses.

For ^{89}Y and ^{93}Nb our initial attempts to fit the data with fixed $V_R(0)$ failed. Therefore, for the final fits shown in Fig. 14 we let $V_R(0)$ be free and fixed a_D at the average of 0.4 fm for the other nuclei with $A > 100$. The fits were achieved by decreasing $V_R(0)$ about 1 MeV such that the valley below the $3p$ peak has been moved up to about 5 MeV. [For given W_D a 1 MeV decrease in $V_R(0)$ shifts the minimum upward 0.8 MeV.] The failure of the initial searches is related to the low observed strengths in the valley.

The most striking result of the study is given by Fig. 17, which shows the imaginary well depths from Figs. 11, 14, and 15. The curve has been drawn visually to fit the points. The point for ^{103}Rh lies far above the curve. Rhodium's flat excitation function (Fig. 14) requires that W_D be large but with large uncertainty because the resonance is much broader than the energy region.

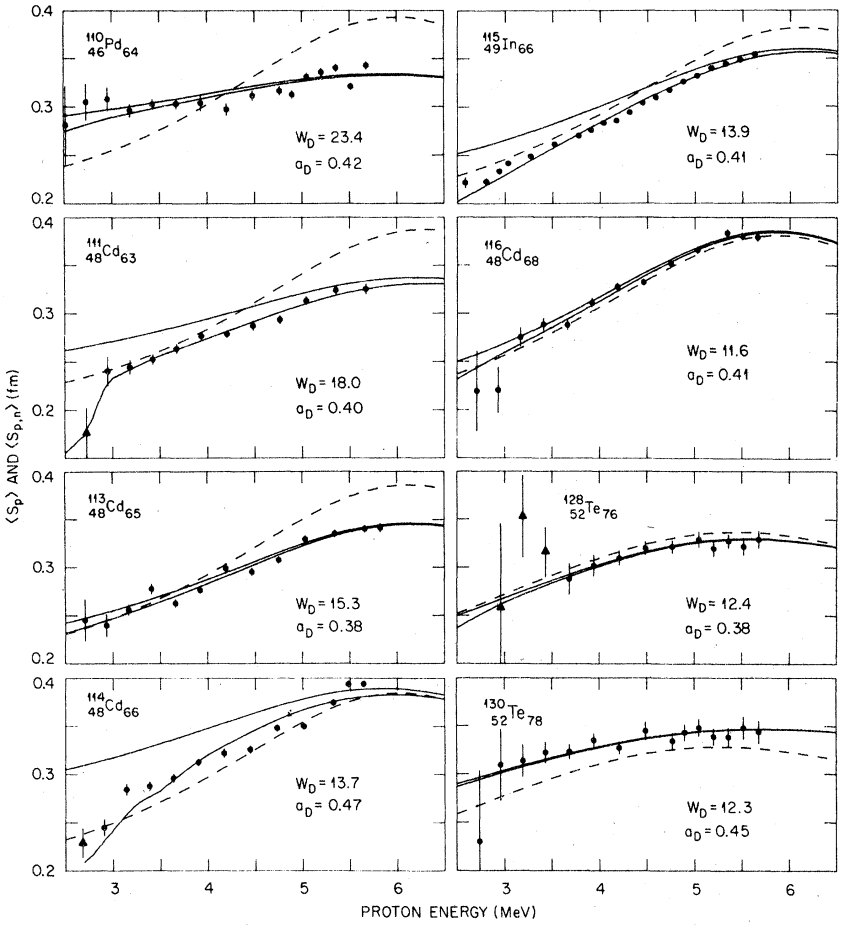

FIG. 15. Reduced (p,n) and total reaction cross sections. See caption for Fig. 14.

G. Targets omitted from the OMP analysis

As stated in Sec. III the yields for four targets, ^{106,108}Pd and ^{125,126}Te, were not analyzed because of uncertainties in target uniformities and background subtraction. But, even though the magni-

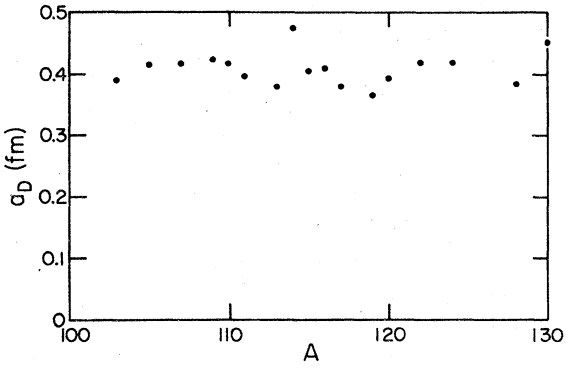

FIG. 16. Fitted values of the imaginary diffuseness for $A > 100$.

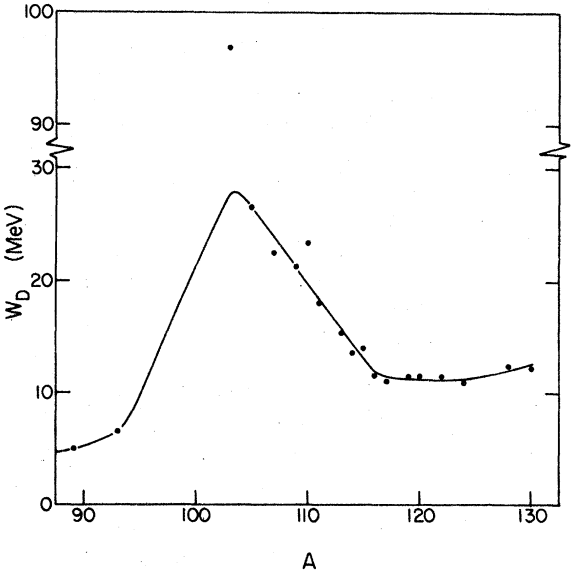

FIG. 17. Fitted values of the imaginary well depth. The curve is drawn visually.

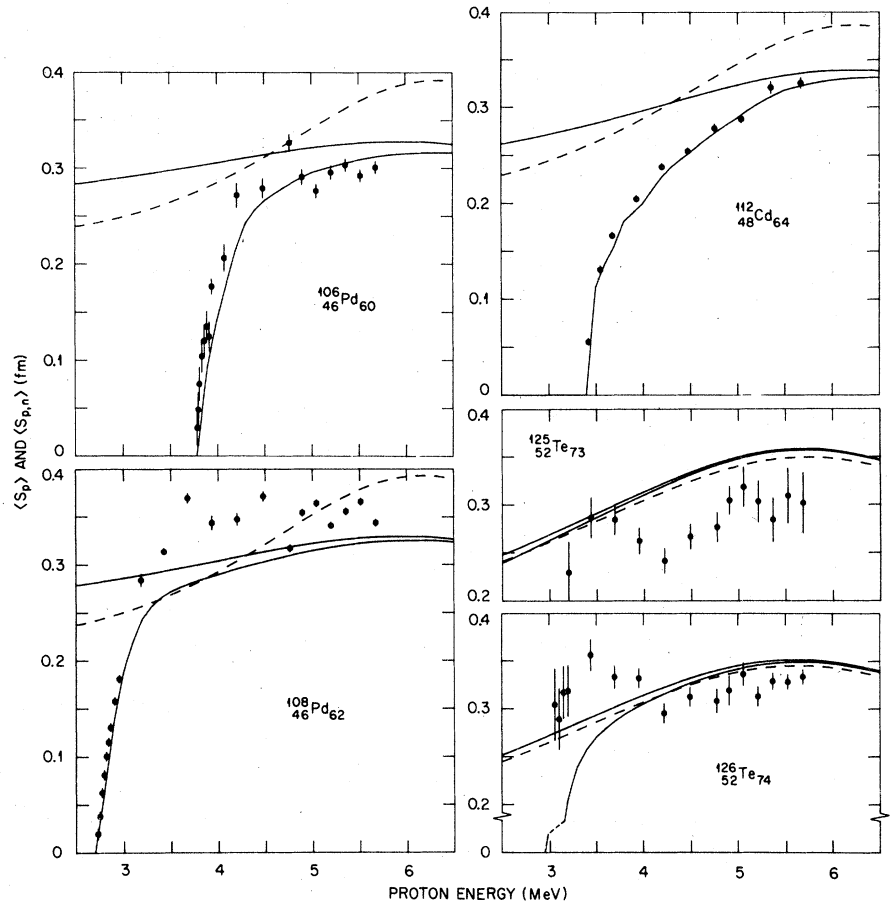

FIG. 18. Reduced cross sections for isotopes not included in the least squares and analyses. The solid curves are analogous to Figs. 14 and 15 except the W_D are taken from the smooth curve in Fig. 17 and $a_D = 0.4$ fm. See the caption for Fig. 14.

tudes of these observed cross sections may not be reliable, the shapes of the excitation functions, at least for energies above 4 MeV, must be consistent with the neighboring nuclei in order to be consistent with the anomalous variations of W_D in Fig. 17. The ^{112}Cd cross sections were also omitted from the analysis because of the large corrections needed for γ-ray emission.

Figure 18 shows the observed $\langle S_{p,n} \rangle$ for these five nuclei and the $\langle S_{p,n} \rangle$ and $\langle S_p \rangle$ predicted using $a_D = 0.4$ fm and using W_D from the smooth curve in Fig. 17. For the dashed curves the imaginary part of the OMP is that of ^{117}Sn, just as in Figs. 14 and 15. The predicted solid curves agree well with the data for ^{112}Cd and are generally consistent with the data for the other nuclei within the errors discussed in Sec. III. The rather flat $\langle S_{p,n} \rangle$ functions observed for ^{106,108}Pd at energies more than 500 keV above the threshold support the conclusion that W_D is large, ~24 MeV, in this mass region.

H. Study of the OMP parameter space

Since the anomalous behavior of W_D in Fig. 17 has not been observed for protons above the Coulomb barrier, we must ask if the anomaly might be avoided by searching in some other region of the OMP parameter space. Although it is difficult to obtain a definitive answer, the following study strongly suggests that the proposed variation in W_D is the simplest way to describe our results. We chose ^{109}Ag for this study because the data are relatively accurate, the Hauser-Feshbach corrections are almost negligible, and the fitted W_D of 21.3 MeV is high up on the anomalous peak. In the six plots of Figs. 19 and 20 the solid curves show the best fit $\langle S_p \rangle$ from Fig. 14 and represent the data. The long dashed curves labeled "zero" are the same as the dashed curve for ^{109}Ag in Fig. 14, as predicted from the ^{117}Sn potential. These "zero" curves are based on rather extensive studies[3] of parameter space for

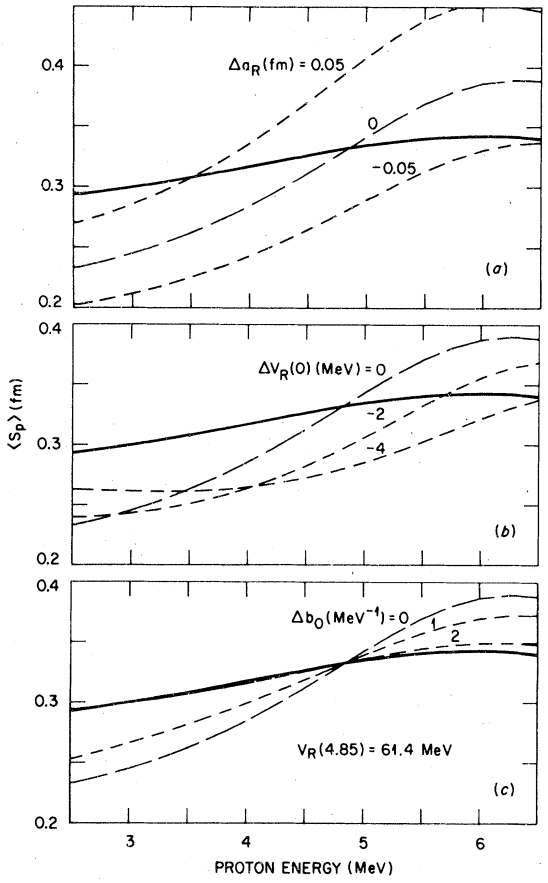

FIG. 19. The effects of parameter variations for ^{109}Ag. In each figure the solid curve is the best fit $\langle S_p \rangle$ for ^{109}Ag from Fig. 14 and represents the data. The dashed "zero" curve is the dashed curve in Fig. 14 predicted from the Sn analysis. The other dashed curves are obtained by changing the listed parameter as indicated. For (c) $V_R(0)$ is also varied to maintain $V_R(E)$ constant at $E = 4.85$ MeV.

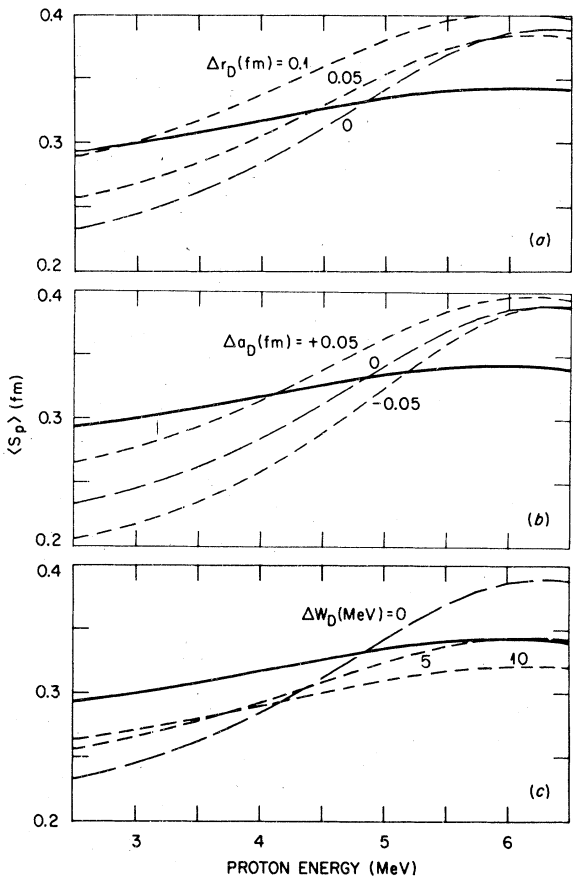

FIG. 20. The effects of parameter variations for ^{109}Ag. (See caption to Fig. 19.)

the accurate Sn data.

In order to avoid the W_D anomaly we need some way to transform the zero curve into the observed solid curve with only small adjustments in the parameters. Basically the curve must be flattened out. Each short-dash curve is produced by changing the indicated parameter from its zero value. Figures 19(a),(b) and 20(a),(b) show that the desired flattening is not achieved by adjusting one of the parameters r_D, a_D, a_R, or $V_R(0)$. A change in $V_R(0)$ shifts the resonance; a change in r_R (not shown) shifts both the resonance and the average magnitude. Both b_0 and $V_R(0)$ are varied in Fig. 19(c); this figure shows that the data could have been fit by a large increase in the slope b_0, from 0.32 to 2.32 MeV^{-1}, with a simultaneous increase in $V_R(0)$ from 62.9 to 72.6 MeV. We pursued this search no further because there seems no reason to replace the anomalous behavior in W_D by larger anomalies in both b_0 and $V_R(0)$. Finally, Fig. 20(c) shows that the resonance is broadened and flattened to about the experimental shape by increasing W_D about 10 MeV from the zero value. The least-squares fit, the solid curve, was achieved by increasing W_D by 9.5 MeV with an associated small increase (10%) in a_D to raise the curve.

I. Comments on the Hauser-Feshbach ratio $F(E)$

One can also ask if the anomaly in W_D might result partly from incorrect predictions in the factor $F(E)$ for converting the observed $\langle \sigma_{p,n} \rangle$ to $\langle \sigma_p \rangle$. This question does not arise for ten targets (^{103}Rh, ^{109}Ag, ^{110}Pd, ^{113,116}Cd, ^{119,122,124}Sn, and ^{128,130}Te) because for these the correction is nearly negligible, i.e., $F(E)$ is nearly unity. There would still be an anomalous decrease in W_D for $A = 103$ to 115 if only those ten points were retained in Fig. 17. The other nine points depend in varying amounts on $F(E)$. For five of them (^{93}Nb, ^{105}Pd, ^{107}Ag, ^{114}Cd, and ^{117}Sn) the predicted

$F(E)$ for the fitted data increased from about 0.72 at low energies to 0.98 at high energies, for ^{111}Cd and ^{120}Sn it increased from about 0.82 to 0.99, and for ^{89}Y from 0.53 to 0.85.

The predictions of $F(E)$ (see Sec. IV A) involve many assumptions and parameters. Ideally the uncertainties in $F(E)$ would be avoided by measuring both (p,γ) and (p,n) cross sections. Alternatively, we can examine the results for internal consistencies. The predicted $F(E)$ produce smoothly varying OMP parameters for isotopes of Pd, Ag, Cd, In, and Sn. For example, ^{107}Ag and ^{109}Ag differ considerably in $\langle\sigma_{p,n}\rangle$ but agree well well in $\langle\sigma_r\rangle$ after the $F(E)$ correction is made to ^{107}Ag (see Fig. 14). Also the calculations of $F(E)$ used to fit ^{89}Y and ^{93}Nb only above excited state thresholds predict the observed excitation functions below those thresholds (see Fig. 14). There is also consistency of ^{89}Y and ^{93}Nb with new data from the University of Kentucky on neighboring nuclei for which $F(E)$ is nearly unity (see Conclusions).

Fortuitously, the error (see Sec. IV C) of omitting the fluctuation correction in the earlier Sn analysis[3] supports the present predictions with fluctuations included. The (p,γ) competition is negligible for ^{122,124}Sn and relatively small for ^{119}Sn, but significant for ^{117,118,120}Sn. With the fluctuations inadvertently omitted, a consistent set of OMP parameters could not be found. Therefore, the $F(E)$ functions were adjusted[3] to force consistency between the OMP parameters for the Sn isotopes that required an $F(E)$ correction and those that did not. Now we find those functions agree with the predictions including fluctuations. Also the new OMP parameters are essentially the same as before.

To examine the uncertainties in the assumptions and corresponding parameters in $F(E)$ for each target would be an exhaustive study. We made a partial study by varying a few parameters for ^{105}Pd for which the $F(E)$ correction is fairly large and the deduced W_D is more than twice that for the Sn isotopes. In accordance with the uncertainties in radiation widths,[28] we varied the γ-ray strength function by ±25% and found a corresponding $^{+20}_{-15}$% variation in W_D. Since an anomaly might exist also for neutrons, we doubled W_D for neutrons and found a 6% increase in W_D for protons. Changing to the neutron potential of Wilmore and Hodgson[50] reduced W_D by 18%. None of these possibilities removes the anomaly for ^{105}Pd.

CONCLUSIONS

By measuring (p,n) cross sections for sub-Coulomb protons we have found that the proton reaction cross sections for $89 < A < 130$ do not follow the systematic trend expected from a proton OMP with parameters chosen to be consistent with the observed[3] resonances in the Sn isotopes. The predicted and observed behavior of the reduced cross sections are summarized respectively by Figs. 1(a) and 1(b) of Sec. I. We find no way to describe these data in the true spirit of the OMP, i.e., with all parameters having only slight and monotonic dependences on N, Z, and A. We have found the simplest procedure is to vary the imaginary well depth W_D, as shown in Fig. 17, with only minor adjustments in the other parameters.

At present, the explanation for these variations is not clear. Perhaps they result from vibrational effects which are particularly strong[51] near $A = 105$. However, vibrational effects should show structure other than the observed smooth A dependence. In particular, the ^{116}Cd nucleus, which is more deformable than the Sn isotopes, might be expected to show a flattened resonance rather than the observed strong energy dependence similar to that in the neighboring Sn nuclei.

Possibly we are observing the shell effects proposed by Lane *et al.*[52] and Lynn[53] to explain anomalies in the neutron strength functions in this mass region. Near closed shells the low density of two-particle, one-hole states available to the incident particle is expected to reduce the absorptive strength W_D. Thus, in Fig. 17 the small W_D near $A = 120$ may result from the 50-proton shell and the lower W_D near $A = 90$ may result from the 50-neutron shell.

Further measurements over broader regions of mass and energy should be very interesting. Currently at the University of Kentucky, Hershberger *et al.*[54] and Flynn *et al.*[55] are measuring both (p,n) total reaction cross sections and proton scattering in this mass region. They have not only confirmed and extended[54] the present work on Ag and In, but also have made extensive new measurements[55] in the mass region $89 < A < 98$ where the present study is inadequate because it includes only two nuclei ^{89}Y and ^{93}Nb, both of which require rather large theoretical corrections to convert the observed $\langle\sigma_{p,n}\rangle$ to total reaction cross section $\langle\sigma_r\rangle$. The OMP deduced here for ^{89}Y and ^{93}Nb has a small W_D, about 6 MeV, and a real well depth such that $\langle S_p\rangle$, the reduced cross section, has a minimum for 5 MeV protons. However, as Fig. 14 shows, the predicted minimum is not seen directly in the reduced (p,n) cross section $\langle S_{p,n}\rangle$. Confidence in the analysis would be increased if we could actually observe the minimum by bombarding neighboring targets for which $\langle\sigma_{p,n}\rangle$ is essentially the total $\langle\sigma_r\rangle$. In fact, Flynn *et al.*[55] ob-

tained such data by bombarding ^{92,94}Zr and ^{95}Mo. For each target they found a broad minimum and deduced an OMP with real and imaginary well depths in agreement with those deduced here for ^{89}Y and ^{93}Nb. Consistent data were obtained also for ^{94,96,98}Mo. Thus, the anomalous behavior of W_D is confirmed.

It would be interesting to extend these measurements below $A=89$ and to compare with the strength functions deduced for $A<65$ from high resolution studies near IAR's by Bilpuch *et al.*[56] However, it is possible that the fine structure studies complement rather than confirm the present type of measurements because of the different dominant partial waves. From ^{92}Mo(p,p) studies, Brandle *et al.*[57] found the dimensionless strength function s_l to be 0.035 ± 0.005 for s waves at 5.3 MeV and 0.02 ± 0.01 for $d_{5/2}$ at 4.3 MeV. Bilpuch *et al.*[58] found the same value for s waves. Both our predicted and fitted potentials in this mass region [Figs. 1(a) and 1(b)] give about 0.031 for s waves and 0.017 for d waves, in agreement with the IAR data. But for p waves the predicted and fitted s_l at 5.3 MeV are 0.048 and 0.027, respectively, and either of these values appear to be consistent with the fine structure studies. [We have approximated s_l by $T_l/(4\pi P_l)$ and, to be consistent with the fine structure work, used $R=1.25\ (1+A^{1/3})$ fm.]

ACKNOWLEDGMENTS

We are grateful to Dr. R. L. Macklin for help and advice in detecting neutrons. We thank Dr. G. R. Satchler and Dr. S. K. Penny for many helpful discussions. We are indebted to E. B. Olszewski and H. L. Adair of the Isotope Division of ORNL for preparation of the enriched targets and to Dr. C. Feldman, H. W. Dunn, and other members of the Analytical Chemistry Division for various analyses of the targets. This work was sponsored by the Division of Basic Energy Sciences, U. S. Department of Energy under Contract No. W-7405-eng-26 with the Union Carbide Corporation.

[1] C. H. Johnson, A. Galonsky, and R. L. Kernell, Phys. Rev. Lett. 39, 1604 (1977).
[2] C. H. Johnson and R. L. Kernell, Phys. Rev. Lett. 23, 20 (1969); Phys. Rev. C 2, 639 (1970).
[3] C. H. Johnson, J. K. Bair, C. M. Jones, S. K. Penny, and D. W. Smith, Phys. Rev. C 15, 196 (1977).
[4] H. S. Camarda, Phys. Rev. C 9, 28 (1974).
[5] J. P. Schiffer and L. L. Lee, Phys. Rev. 107, 640 (1957); 109, 2098 (1958).
[6] A. J. Elwyn, A. Marinov, and J. P. Schiffer, Phys. Rev. 145, 957 (1966). The reduced cross section presented in this paper should be divided by 2 to be consistent with the present work.
[7] C. H. Johnson, C. C. Trail, and A. Galonsky, Phys. Rev. 136, B1719 (1964).
[8] C. H. Johnson, R. L. Kernell, and S. Ramavataram, Nucl. Phys. A107, 21 (1968).
[9] C. H. Johnson and R. L. Kernell, Phys. Rev. 169, 974 (1968).
[10] R. L. Macklin, Nucl. Instrum. 1, 335 (1957).
[11] A. DeVolpi and K. G. Porges, Phys. Rev. C 1, 683 (1970).
[12] J. H. Gibbons and R. L. Macklin, Phys. Rev. 114, 571 (1959).
[13] M. E. Anderson, Nucl. Appl. Technol. 4, 142 (1968).
[14] J. K. Bair and H. Butler, private communication.
[15] D. M. Fleming and I. T. Myers, Intern. J. Appl. Radiat. Isot. 17, 251 (1966).
[16] J. L. Fowler, C. H. Johnson, and R. M. Feezel, Phys. Rev. C 8, 545 (1973).
[17] A. H. Wapstra and K. Bos, At. Data Nucl. Data Tables 19, 215 (1977).
[18] H. H. Andersen, C. C. Hanke, H. Sorensen, and P. Vajda, Phys. Rev. 153, 338 (1967).
[19] E. Finckh and U. Jahnke, Nucl. Phys. A111, 338 (1968).
[20] W. J. Courtney and J. D. Fox, At. Data Nucl. Data Tables 15, 141 (1975).
[21] D. L. Dittner and W. W. Daehnick, Phys. Rev. 188, 1881 (1969).
[22] D. Robson, Phys. Rev. 137, B535 (1965).
[23] R. L. Kernell and C. H. Johnson, Bull. Am. Phys. Soc. 11, 630 (1966).
[24] M. Harchol, S. Cochavi, A. A. Jaffe, and C. Drory, Nucl. Phys. 79, 165 (1966).
[25] W. Hauser and H. Feshbach, Phys. Rev. 87, 366 (1952).
[26] S. K. Penny, private communication.
[27] P. A. Moldauer, Nucl. Phys. 47, 65 (1963).
[28] C. H. Johnson, Phys. Rev. C 16, 2238 (1977).
[29] R. L. Auble, Nucl. Data Sheets B7, 465 (1972); B8, 77 (1972); 9, 125 and 157 (1973); 25, 315 (1978).
[30] R. L. Auble, H. R. Hiddleston, and C. P. Browne, Nucl. Data Sheets 17, 573 (1976).
[31] F. E. Bertrand, Nucl. Data Sheets B7, 33 (1972); 11, 449 (1974); 13, 397 (1974); 22, 135 (1977); 23, 229 (1978).
[32] F. E. Bertrand and D. J. Horen, Nucl. Data Sheets B7, 1 (1972).
[33] G. A. Carlson, W. L. Talbert, Jr., and S. Raman, Nucl. Data Sheets 14, 247 (1975).
[34] H. R. Hiddleston and C. P. Browne, Nucl. Data Sheets 13, 133 (1974).
[35] D. J. Horen, Nucl. Data Sheets B8, 123 (1972); 13, 133 (1974).
[36] H. J. Kim, Nucl. Data Sheets 16, 107 (1975).
[37] D. C. Kocker, Nucl. Data Sheets B8, 527 (1972); 10, 241 (1973); 13, 337 (1974); 16, 55 and 445 (1975).
[38] S. Raman and H. J. Kim, Nucl. Data Sheets B5, 181 (1971); B6, 39 (1971); B7, 69 (1972); 16, 195 (1975).
[39] L. E. Samuelson, W. H. Kelly, R. L. Auble, and W. C. McHarris, Nucl. Data Sheets 18, 125 (1976).

[40]R. E. Anderson, R. L. Bunting, J. D. Burch, S. R. Chinn, J. J. Kraushaar, R. J. Peterson, D. E. Prull, B. W. Ridley, and R. A. Ristinen, Nucl. Phys. A242, 93 (1975).
[41]D. A. Hutcheon and D. R. Gill, Nucl. Phys. A248, 397 (1975).
[42]H. J. Kim and R. L. Robinson, Phys. Rev. C 9, 767 (1974).
[43]D. Rabenstein and D. Harrach, Nucl. Phys. A242, 189 (1975).
[44]W. Dietrich and A. Backlin, Physik A276, 133 (1976).
[45]W. Dilg, W. Schantl, H. Vonach, and M. Uhl, Nucl. Phys. A217, 269 (1973).
[46]J. A. Holmes, S. E. Woosley, W. A. Fowler, and B. A. Zimmerman, At. Data Nucl. Data Tables 18, 305 (1976).
[47]P. A. Moldauer, Phys. Rev. 135, B642 (1964).
[48]G. R. Satchler, in *Isospin in Nuclear Physics*, edited by D. H. Wilkinson (North-Holland, Amsterdam, 1969), Chap. 9.
[49]F. G. Perey, private communication.
[50]D. Wilmore and P. E. Hodgson, Nucl. Phys. 55, 673 (1964).
[51]P. H. Stelson and L. Grodzins, Nucl. Data, Sect. A1, 21 (1965).
[52]A. M. Lane, J. E. Lynn, E. Melkonian, and E. R. Rae, Phys. Rev. Lett. 2, 424 (1959).
[53]J. E. Lynn, *Theory of Neutron Resonance Reactions* (Clarendon, Oxford, England, 1968), p. 288.
[54]R. L. Hershberger, D. S. Flynn, F. Gabbard, and C. H. Johnson (to be published).
[55]D. S. Flynn, R. L. Hershberger, and F. Gabbard (to be published).
[56]E. G. Bilpuch, A. M. Lane, G. E. Mitchell, and J. D. Moses, Phys. Rep. 28C, 145 (1976).
[57]H. Brandle, V. Meyer, and M. Salzmann, Nucl. Phys. A256, 141 (1976).
[58]E. G. Bilpuch, J. D. Moses, F. O. Purser, H. W. Newson, G. E. Mitchell, R. O. Nelson, and D. A. Outlaw, Phys. Rev. C 9, 1589 (1974).